

THE WATER ABUNDANCE OF THE DIRECTLY IMAGED SUBSTELLAR COMPANION κ AND b RETRIEVED FROM A NEAR INFRARED SPECTRUM

KAMEN O. TODOROV¹, MICHAEL R. LINE², JAIME E. PINEDA^{1,3}, MICHAEL R. MEYER¹, SASCHA P. QUANZ¹, SASHA HINKLEY⁴, JONATHAN J. FORTNEY²

Draft version September 8, 2021

ABSTRACT

Spectral retrieval has proven to be a powerful tool for constraining the physical properties and atmospheric compositions of extrasolar planet atmospheres from observed spectra, primarily for transiting objects but also for directly imaged planets and brown dwarfs. Despite its strengths, this approach has been applied to only about a dozen targets. Determining the abundances of the main carbon and oxygen-bearing compounds in a planetary atmosphere can lead to the C/O ratio of the object, which is crucial in understanding its formation and migration history. We present a retrieval analysis on the published near-infrared spectrum of κ And b, a directly imaged substellar companion to a young B9 star. We fit the emission spectrum model utilizing a Markov Chain Monte Carlo algorithm. We estimate the abundance of water vapor, and its uncertainty, in the atmosphere of the object. In addition, we place an upper limit on the abundance of CH₄. We compare qualitatively our results to studies that have applied model retrieval on multiband photometry and emission spectroscopy of hot Jupiters (extrasolar giant planets with orbital periods of several days) and the directly imaged giant planet HR 8799b.

Subject headings: stars: planetary systems — direct imaging — techniques: spectroscopic — methods: data analysis — planets and satellites: individual (κ And b)

1. INTRODUCTION

The study of exoplanets is moving from an era focussed on discovery to one of characterization. While most exoplanets detected to date have been discovered through the radial velocity or transit techniques, there are a handful of substellar companions within ~ 100 AU of their host stars discovered through direct imaging (Pepe et al. 2014). It remains unclear whether these populations are distinct or can be considered as part of a continuum of objects drawn from a variety of formation mechanisms, and experiencing a range of evolutionary histories.

The compositions of transiting and directly imaged extrasolar giant planets may be an important marker of their formation and migration history (Öberg et al. 2011; Madhusudhan et al. 2014a). These authors suggest that giant planets' C/O and C/H ratios are affected by the locations in the protoplanetary disks where they formed with respect to the water and CO ice lines, as well as by the formation mechanism. E.g., Öberg et al. (2011) suggest that stellar C/O and C/H ratios are indicative of either formation within the water ice line or via gravitational instability. Substellar C/O, but superstellar C/H point to significant accretion of water ice bodies after the gas accretion phase. Superstellar C/O and C/H can mean gas accumulation near the CO or CO₂ ice lines or significant accretion of carbon grains. Superstellar C/O and substellar C/H indicates gas accretion from outside

the water snow line. A caveat is that Öberg et al. (2011) assume that the planet forms at a fixed location within the disk and do not consider the impact of disk migration.

The emission and absorption spectra of giant exoplanets and substellar companions can inform us about the chemical species and the C/O ratio in their atmospheres and help resolve the debate about their formation mechanism and evolution. Two complementary approaches have been used in constraining the atmospheric structure and composition of these objects. The first one relies on sophisticated forward modeling of the physical and chemical processes in the atmospheres of giant planets and calculating molecular abundances and pressure-temperature (P-T) profiles, and subsequently computing the resulting spectra (e.g., Fortney et al. 2006, 2008; Burrows et al. 2007, 2008). This approach, however, is computationally expensive, which combined with the large number of free parameters makes it extremely difficult to compare the model spectra to observations in a statistically robust manner. While model spectra that match the data can be found, quantifying the uncertainties in the underlying individual parameters is difficult.

The other approach, “spectral retrieval”, on which we focus here, relies on a simple radiative transfer model that assumes that the P-T profile, the surface gravity and the atmospheric composition (with only few main molecular species considered) are free parameters (e.g., Benneke & Seager 2012, 2013; Lee et al. 2012; Line et al. 2012, 2013; Heng & Lyons 2016). The effects of clouds on substellar emission spectra can also be parametrized and included (e.g., Madhusudhan et al. 2011; Lee et al. 2013, 2014a,b). Model spectra produced in this way are computationally cheap and the limited number of parameters makes fitting to observations feasible. Since the

¹ Institute for Astronomy, ETH Zürich, Wolfgang-Pauli-Strasse 27, 8093 Zürich, Switzerland

² Department of Astronomy & Astrophysics, University of California, Santa Cruz, Santa Cruz, CA 95064, USA

³ Current address: Max Planck Institute for Extraterrestrial Physics, 85748 Garching, Germany

⁴ School of Physics, University of Exeter, Stocker Road, Exeter, EX4 4QL

physical phenomena included in these models are limited, they rely entirely on observational data to inform the fit, although priors based on theoretical considerations can improve the retrieval. A caveat is that the models used for retrieval, while still accounting for the most important physical processes and chemical species, could still be over-simplistic. Thus, not all features of a given atmosphere may be accounted for correctly.

In this study, we examine an integral field near-infrared spectrum observed by [Hinkley et al. \(2013\)](#) of the directly imaged substellar companion orbiting the young star κ Andromedae (hereafter κ And b following [Carson et al. 2013](#)). We summarize the known properties of the κ And system in Section 2. In Section 3, we discuss the available observed spectrum of κ And b. We present our simple atmospheric model in Section 4. Section 5 focuses on our spectral retrieval approach, and in Section 6 we discuss our results and compare them to similar studies of giant hot exoplanets.

2. KNOWN PROPERTIES OF THE κ ANDROMEDAE SYSTEM

κ Andromedae is a young but already post-main sequence B9IVn star ([Wu et al. 2011](#)) whose accurate age is debated. [Carson et al. \(2013\)](#), who discovered the companion, assume that κ And is a member of the Columba association ([Zuckerman et al. 2011](#)) and, following [Marois et al. \(2010\)](#), adopt an age of 30_{-10}^{+20} Myr for their analysis. On the other hand, [Hinkley et al. \(2013\)](#) use theoretical stellar isochrone tracks ([Bertelli et al. 2009](#)) combined with the previously measured stellar properties to derive an age of 220 ± 100 Myr. An alternative analysis by [Bonnefoy et al. \(2014\)](#) adopts a more conservative value than [Carson et al. \(2013\)](#), but still based on the age of the Columba association: 30_{-10}^{+120} Myr. The correct age of the system is important when assessing the luminosity and hence the mass of κ And b, whose spectral type is $L1 \pm 1$ ([Hinkley et al. 2013](#)). There is no available dynamical mass estimate for this object. [Carson et al. \(2013\)](#) use their estimate for the age of the system (30_{-10}^{+20} Myr) and the DUSTY evolutionary models ([Allard et al. 2011](#)) to estimate a companion mass of $12.8_{-1.0}^{+2.0} M_J$. On the other hand, [Hinkley et al. \(2013\)](#) adopt $M_{\text{comp}} = 50_{-13}^{+16} M_J$, while [Bonnefoy et al. \(2014\)](#) place a lower limit on the mass of the object of $M_{\text{comp}} > 10 M_J$ based on “warm-start” evolutionary models. While in principle it is a basic parameter, the mass of the companion is of secondary importance for our purposes, because it enters the spectrum formation only via the surface gravity term, which also depends on the radius of the object. The effective temperature of κ And b is 2040 ± 60 K ([Hinkley et al. 2013](#)). We summarize the known properties of the host star and its companion in Table 1.

3. OBSERVATIONS

In our analysis, we consider the spectrum of κ And b as published by [Hinkley et al. \(2013\)](#). We offer a brief summary of how the data were obtained. These authors used the “Project 1640” instrument ([Hinkley et al. 2011](#); [Openheimer et al. 2012](#)) on the 200 inch Hale Telescope at Palomar Observatory. Project 1640 is an integrated combination of a coronagraph and an integral field spec-

trograph (IFS) and covers the Y, J and H bands. The data were obtained on UT 2012 December 23, starting at an airmass of 1.02. A total of 16 images were taken with exposures of 183 s each, with the Hale Telescope adaptive optics on, and the star hidden behind the coronagraphic mask. The spectrum extraction is described in detail in [Hinkley et al. \(2013\)](#). The observations cover the range between 0.9 and $1.8 \mu\text{m}$, but for this study, we focus on wavelengths longer than $1 \mu\text{m}$. At shorter wavelengths, the molecules that we consider (CH_4 , CO , CO_2 , H_2O , C_2H_2 , HCN , NH_3 , see Section 4) and the P-T profile have a limited impact on the emission spectrum (e.g., [Lee et al. 2014a](#)). The spectrum is low-resolution ($R \approx 45$) and contains 28 flux points in the range we examine. The uncertainties derived by the observers for every spectroscopic channel include the uncertainties due to photon noise, systematic errors and uncertainties resulting from the spectral calibration. Unfortunately, the absolute calibration of the resulting flux values is not precise, and therefore it is difficult to derive the radius of the companion from its luminosity using the well known distance to κ And (52 ± 2 pc from *Hipparcos* parallaxes; [Perryman et al. 1997](#); [Carson et al. 2013](#)).

4. ATMOSPHERIC EMISSION MODEL

4.1. General Description

For this study we require a relatively fast and therefore relatively simple radiative transfer code that takes a limited number of parameters – chemical species volume mixing ratios, P-T profile and a scaling factor that incorporates the companion’s distance and luminosity – and computes an emission spectrum. To this end, we implement a custom one-dimensional plane-parallel atmospheric model that we validate against the results from the NEMESIS code ([Irwin et al. 2008](#)) and the spectral synthesis software used by [Line et al. \(2012\)](#) and [Line et al. \(2013\)](#). These codes were designed to study the spectra of planets, including hot Jupiters and young directly imaged gas giants. While we occasionally refer to them as “radiative transfer” models for simplicity, we do not enforce radiative equilibrium in our code, since κ And b is a self-luminous object releasing its primordial heat of accretion. Due to its separation from the primary, the companion is negligibly externally heated.

Following [Line et al. \(2012\)](#), we consider the effects of nine chemical species on the emission spectrum in our radiative transfer model: CH_4 , CO , CO_2 , H_2O , H_2 and He , as well as C_2H_2 , HCN and NH_3 . The first four are expected to be the major sources of molecular line opacity in a hot substellar atmosphere (e.g., [Tinetti et al. 2007](#); [Swain et al. 2009](#)). Other relatively common molecules also have absorption bands in the wavelength range we consider, e.g. hydrogen cyanide (HCN), acetylene (C_2H_2) and ammonia (NH_3 ; e.g., [Rothman et al. 2009](#)). The abundances of these species in self-luminous gas giant planets and brown dwarfs are expected to be much lower compared to the abundances of water, carbon monoxide, carbon dioxide and methane (e.g., [Lodders & Fegley 2002](#); [Zahnle & Marley 2014](#)), but nevertheless could have an impact on the emitted spectrum and therefore we explore models that include these three species. Alkali metal atomic species, e.g., K I and Na I , have some lines that fall within the wavelength range we consider.

Table 1
Stellar and Companion Parameters for the κ And System

M_* (M_\odot)	2.4 – 2.5	Carson et al. (2013)
J_* (mag) [†]	4.624 ± 0.264	2MASS, Skrutskie et al. (2006)
H_* (mag) [†]	4.595 ± 0.218	2MASS, Skrutskie et al. (2006)
$K_{s,*}$ (mag) [†]	4.571 ± 0.354	2MASS, Skrutskie et al. (2006)
$T_{\text{eff},*}$ (K)	10730 ± 250	Wu et al. (2011)
SpT _*	B9IVn	Wu et al. (2011)
Distance (pc)	52 ± 2	<i>Hipparcos</i> ; Perryman et al. (1997); Carson et al. (2013)
J_{comp} (mag)	16.3 ± 0.3	Carson et al. (2013)
H_{comp} (mag)	15.2 ± 0.2	Carson et al. (2013)
$K_{s,\text{comp}}$ (mag)	14.6 ± 0.4	Carson et al. (2013)
L'_{comp} (mag)	13.12 ± 0.09	Carson et al. (2013)
$T_{\text{eff,comp}}$ (K)	2040 ± 60	Hinkley et al. (2013)
Projected separation (")	1.064 ± 0.006	Carson et al. (2013)
Projected separation (AU)	56 ± 2	Carson et al. (2013)
Position angle (°)	55.9 ± 0.4	Carson et al. (2013)

[†] Two Micron All Sky Survey (2MASS) magnitude of the star (from the Infrared Science Archive: <http://irsa.ipac.caltech.edu>).

To investigate this, we compare the κ And observation with an observation from the SpeX Prism Spectral Libraries⁵ of a L2.5 brown dwarf with similar effective temperature (2MASS J14343616+2202463; Sheppard & Cushing 2009). In a typical example, it is possible that the κ And b observation at 1.14 μm is affected by a Na I line doublet. However, we would need signal to noise 3-5 times higher to be able to make this claim. Thus, due to the limited resolution and large uncertainties of our data, neutral atomic alkali lines are unlikely to have a significant impact on our results.

For CO, CO₂, H₂O we adopt opacities from the HITEMP database (Rothman et al. 2010). For methane, acetylene, hydrogen cyanide and ammonia, we adopt the opacities from Freedman et al. (2014). In addition, we include the collision induced opacity due to H₂-H₂ and H₂-He interactions (Borysow et al. 2001; Borysow 2002). The adopted opacities cover the temperature range between 500 and 3000 K and the pressure range between 10⁻⁶ and 10² bar. The line-by-line cross section databases as a function of T and P are sampled at a resolution of 1 cm⁻¹. Throughout this study, we consider the abundance of each species as a fraction of the total number of molecules. The CH₄, CO, CO₂ and H₂O abundances are free parameters in all of our fits. We run fits with the abundances of C₂H₂, HCN, NH₃ all fixed at zero or all set to be free. The ratio between H₂ and He is fixed to 86:14 (Line et al. 2012). The mean molecular weight of the atmosphere is calculated based on these main chemical species, assuming that the contribution from other molecules is small.

In our model, the atmosphere is divided into a number of horizontal layers as a function of pressure. In this study, we use 90 layers that are evenly spaced in $\log(P)$, varying between 2.4×10^{-6} and 163.3 bar. Each layer has a temperature, based on the input P-T profile and a chemical composition associated with it. Following Line et al. (2012), we keep the relative abundances by number of all molecules we consider uniform for all layers, since the information content of the spectrum is insufficient to allow the retrieval of chemical gradients. We calculate the amount of flux from a given layer that leaves

the atmosphere unimpeded and integrate over all layers, for a given wavelength. In other words, like Line et al. (2012), we follow, e.g., Gray (2005) and compute, for each atmospheric layer, the change in optical depth,

$$\Delta\tau_{i,\lambda} = \frac{\Delta P_i}{\mu g} \sum_{k=0}^N (\sigma_{\lambda,k} f_{\lambda,k}), \quad (1)$$

where ΔP_i is the change in pressure in the i^{th} layer (in units of barye, i.e., g cm⁻¹ s⁻²); μ (in g mol⁻¹) and g (in cms²) are the mean molecular weight and the surface gravity, respectively. $\sigma_{\lambda,k}$ (in cm²) and $f_{\lambda,k}$ are the molecular cross-section at wavelength λ and mixing ratio of the k^{th} chemical species, respectively. We integrate this value over all layers lying above the i^{th} layer to calculate the total amount of optical depth, $\tau_{i,\lambda}$, that a photon emitted from this layer would encounter. Since some of the light emitted by any given layer will be absorbed within that layer, we account for this effect by dividing the i^{th} layer in upper and lower half in pressure by dividing ΔP_i by two and adding the $\Delta\tau_{i,\lambda}$ value of the upper half to $\tau_{i,\lambda}$. The emitted intensity of a ray of light through the atmosphere is then,

$$I_\lambda = \sum_{i=1}^{90} B(T_i, \lambda) e^{-\tau_{i,\lambda}/\cos(\theta)} \frac{\tau_{i,\lambda}}{\cos(\theta)}, \quad (2)$$

where B is the Planck black body radiation at temperature T_i and θ is the angle between the direction to the observer and the normal to the surface. In order to get the observable flux, we integrate this over the visible surface of the planet,

$$F_\lambda = \int_0^{2\pi} \int_0^\pi I_\lambda \cos(\theta) d\theta d\phi, \quad (3)$$

To compute this integral efficiently, we take advantage of the Gaussian quadrature approximation. The same operation is performed for every wavelength in which we are interested between 1 and 1.8 μm . The layers at the top of the atmosphere have too low optical depths to have a significant impact on the spectrum in the near-infrared, while the layers near the bottom are too obscured by the

⁵ <http://pono.ucsd.edu/~adam/browndwarfs/spexprism/>

opacity of the upper layers (the top 10 and bottom 10 layers have $< 0.001\%$ contribution to the total flux).

We sample the model spectrum at a resolution 50 times higher than that of the observed spectrum – every $\sim 3 \text{ cm}^{-1}$, or $\sim 6 \text{ \AA}$ in this wavelength range. The model emitted flux is binned in wavelength to match the resolution of the observed spectrum. This approach is similar to the methods of Line et al. (2012) and Line et al. (2013). Since the molecular opacity data is sampled at 1 cm^{-1} , finer sampling than that will not improve the information content of our model. Sampling our model spectrum at full 1 cm^{-1} resolution slows down the model calculation by a factor of three compared to sampling at our choice of 3 cm^{-1} and makes Bayesian fitting impractical. To ensure robustness, we produce test model spectra sampled at 1 cm^{-1} and 3 cm^{-1} for several arbitrary but reasonable parameter combinations and find that, after binning the models to the resolution of the data, they are different by $\lesssim 1\%$ per spectroscopic point, much less than the uncertainties of the observed spectrum. Therefore, our choice of wavelength sampling of the models does not impact our results.

4.2. Treatment of Clouds

Previous emission spectrum retrieval studies have treated clouds and hazes (Lee et al. 2013, 2014a,b). These authors have explored cloudless and uniformly cloudy (the atmosphere being uniformly permeated by particles of a given size) models as well as an “intermediate” model, where the cloud layer has a minimum and maximum pressure, similarly to Burrows et al. (2011). Lee et al. (2014a) have discussed aerosol treatment in detail and included it in their retrieval for the transit spectrum of HD 189733b by varying the wavelength dependent number density of the aerosol particles and their size. We adopt a more numerically simplified approach, choosing to parametrize the macroscopic quantity of cloud optical depth instead of the microscopic quantities of cloud particle opacity and number density. Since our radiative transfer code is one-dimensional, we consider a single cloud layer that covers the whole planet with no gaps. The clouds are represented by adding “grey opacity” to the molecular opacities in the atmospheric layers in the model where the cloud occurs. This is usually equivalent to assuming that the cloud particles are much larger than the observation wavelength, but since we consider a relatively narrow wavelength range between 1 and $1.8 \mu\text{m}$, there are cloud chemical species that would appear approximately grey even if their particles are comparable in size to the observed wavelength (e.g., Morley et al. 2012; Lee et al. 2013). The amount of radiation that passes through the cloud is determined by the amount of extra optical depth contained in the “cloudy” atmospheric layers. The optical depth contribution from the cloud deck is invariant with wavelength. We describe the optical depth contribution of the cloud deck as a Gaussian as a function of pressure in log space, similarly to Heng et al. (2012). The altitude of the deck (i.e., the pressure at the location of the peak of the Gaussian), the peak optical depth contribution of the cloud and the vertical extent of the cloud are emission model inputs and can be explored by the fitting routine as free parameters. This scheme is illustrated in Figure 1. It

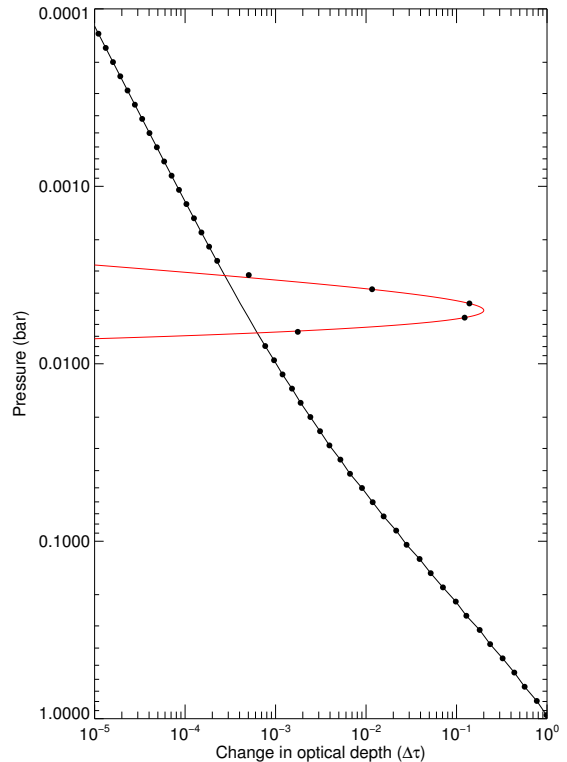


Figure 1. We show a *schematic* representation of our cloud treatment approach for an arbitrary combination of molecular mixing ratios and at an arbitrary wavelength. The relation between pressure and optical depth is represented by the black line. The red line is a Gaussian describing the contribution to the change in optical depth due to the cloud layer. The pressure at the peak of the Gaussian, its amplitude and standard deviation are free parameters in the fit. The black points show the total change in optical depth in a given atmospheric layer.

is possible that the cloud permeates a “wide” range of pressures, i.e., the standard deviation of the Gaussian optical depth contribution is so large that the Gaussian is in essence flat in our region of interest. This case would be equivalent to the uniformly cloudy model in Lee et al. (2013, 2014b).

For simplicity, we do not include the effect of scattering that will effectively reduce the “apparent” opacity. Forward scattering particles will transport more light through the top of the cloud, which is the equivalent of reducing the cloud opacity in pure absorption. Thus, scattering and cloud opacity will be degenerate in our simple framework. For a detailed theoretical discussion of clouds in brown dwarfs and young planets, see Morley et al. (2012).

5. FITTING PROCEDURE

5.1. Free Parameters

We explore four cases of the model fit to the observed spectrum – 1) without clouds and only including the four main molecules: CH_4 , CO , CO_2 and H_2O ; 2) cloudy and only including the four main molecules; 3) cloud-free, including the four main molecules plus the three additional ones: C_2H_2 , HCN , NH_3 ; and 4) cloudy and all seven considered molecules. We summarize the parameters and their definition in Table 2. For each case, we indicate which parameters are left free and which are fixed at 0. The spectrum model requires that 90 layers in pressure and temperature are specified. However, the

temperature cannot be let to vary freely in each layer, because the spectrum does not contain sufficient information for this – even neglecting the signal-to-noise considerations, there would be more than 90 free parameters compared to a spectrum of 28 points. We select nine individual layers, uniformly interspersed in pressure, where the temperatures are free parameters ($T_1 - T_9$). We then use quadratic interpolation to determine the temperature values for the 81 remaining layers between these points. In order to test whether a 9-point P-T profile is reasonable, we run two MCMC chains (one million iterations each) with clouds turned off and by fixing $\log(g_{surf}) = 4.5$ using a 7-point and a 12-point P-T profile. We find that the molecular volume mixing ratio values resulting from these are consistent with the MCMCs using a 9-point model well within 1σ .

The surface gravity of the companion, g_{surf} , is uncertain, and expected to be correlated with the molecular abundances. High surface gravity flattens the spectrum and requires a higher abundance of a molecular species to produce a feature of a given depth. Thus, fixing the surface gravity to a “reasonable” value would result in chemical abundance estimates with inaccurate uncertainties. Hence, even though we cannot constrain this property, we leave it as a free parameter in all four cases that we explore in detail, such that $\log(g_{surf}) \in (3.5, 5.2)$, in cgs. We pick this interval based on estimates of the surface gravity of κ And b from [Hinkley et al. \(2013\)](#).

While the relative flux from point to point within the spectrum is well calibrated, the absolute flux calibration is uncertain. To compensate for this and for the unknown radius of κ And b, we introduce a multiplicative term, $A_{calib} \sim \frac{R_{comp}^2}{d^2} G_{conv}$, where G_{conv} is the unknown conversion factor between measured and “true” flux. R_{comp} is the radius of the companion and d is the distance to the κ And system.

5.2. Markov Chain Monte Carlo

As a first step in the fitting process, we employ the IDL MPFIT χ^2 -minimization library ([Markwardt 2009](#)) to provide us with an initial guess about the location of the minimum χ^2 in the free parameter space. Then, we employ a Markov Chain Monte Carlo (MCMC) approach to get best fit values and uncertainties. For this analysis, we have utilized the MCMC algorithm implemented and described by [Todorov et al. \(2012, 2014\)](#), who follow [Ford \(2005, 2006\)](#). We use the Metropolis-Hastings algorithm within the Gibbs sampler in conjunction with a Gaussian trial value probability distribution. We assume flat priors for all parameters. During a given MCMC iteration, we perturb only a single randomly chosen free parameter. Each MCMC chain that we execute has 10^6 iterations, or approximately 50,000-70,000 iterations per parameter. The initial part of the MCMC chain (10% or 10^5 iterations) is discarded as “burn-in” time necessary for the algorithm to converge. Before running a long chain, we run shorter chains in order to choose the “step sizes”, i.e., the standard deviations of the Gaussian probability distributions used to select the amount by which a given parameter is perturbed. In order to optimize the convergence speed of the chain, we select, by experimentation, the Gaussian widths such that the acceptance rate of the given parameter is between 15 and 35%. We constrain

the molecular number fractions of the molecules to be less than 10^{-1} and the temperatures are constrained to be less than 3000 K by preventing any trial states that exceed these values. This is done in order to prevent the chains from entering temperature regimes where the opacities are not defined and preventing the total abundance of the molecules included in the fit from becoming unrealistically large.

6. RESULTS AND DISCUSSION

6.1. Adopted Parameter Values and Uncertainty Estimation

As discussed in Section 5.1, we run an MCMC chain for each of the four cases we consider – cloudy vs. cloud-free and four main molecules vs. all seven species in the model atmosphere. For all chains, the best fit model is chosen as the model with the minimum χ^2 value in the MCMC chain, after the initial 10^5 iterations have been dropped as mentioned before. While this model best fits the available data, its parameters are not necessarily the values on which the MCMC converges finally. We find that the reduced χ^2 values for the fits are 1.25, 2.21, 1.13 and 2.06 for cases 1-4 (as defined in Table 2), respectively. The corresponding Bayesian information criterion (BIC) values are 66.1, 82.1, 71.3 and 84.4. Even though the reduced χ^2 values of the best fit models that the four-species chains encountered are larger than the values produced by the seven-species fits, the BIC values for the latter models are significantly larger. Similarly, cloud-free BIC values are much smaller than cloudy ones. This suggests that the improvements in the fit achieved by adding molecules and clouds are not significant given the extra free parameters in the model, and for our results discussion, we adopt the outcome of the chain with the minimum BIC, case 1: cloud-free, including only CH_4 , CO , CO_2 and H_2O . We compare the best-fitting emission models from this MCMC run to the data in Figure 2.

The surface gravity does not converge in any of the tested chains and the MCMC histograms for this parameter are flat. Therefore, we are unable to place any constraints on it.

We present the P-T profiles for case 1 in Figure 3, and for all cases in the Appendix, Figure 8. Several percent of the P-T profiles tested, especially for case 3, cloud-free with seven molecules, exhibit sharp temperature inversions. We find that the affected model atmospheres contain very little water ($\log(n_{\text{H}_2\text{O}}) \lesssim -6$) but the abundances of other molecules tend to be large (methane, CO and CO_2 have $\log(n) \gtrsim -2.5$). The temperature inversions cause these molecules to appear in emission instead of absorption. Since there is no water in these models, there is a trough (in emission) near 1.4 μm , while on either side the CO , CO_2 and CH_4 can be seen in emission. The overall flux level of the spectrum is then compensated by the A_{calib} free parameter (Table 2). At the resolution of the observations, this configuration closely resembles the observed spectrum. The inverted P-T profiles represent likely unphysical states of our vector of free parameters, considering the strength of the required temperature inversion, that nevertheless result in spectra similar to the observed. This underscores the importance of high-resolution spectra of substellar

Table 2
Parameters of the Fit

Parameter (units)	Case 1 ^a	Case 2 ^b	Case 3 ^c	Case 4 ^d	Description
<i>Main molecules</i>					
n _{H₂O}	free	free	free	free	Water molecules number fraction.
n _{CH₄}	free	free	free	free	Methane molecules number fraction.
n _{CO}	free	free	free	free	CO molecules number fraction.
n _{CO₂}	free	free	free	free	CO ₂ molecules number fraction.
<i>Other molecules</i>					
n _{C₂H₂}	0	0	free	free	C ₂ H ₂ molecules number fraction.
n _{HCN}	0	0	free	free	HCN molecules number fraction.
n _{NH₃}	0	0	free	free	NH ₃ molecules number fraction.
<i>Cloud parameters</i>					
C _{amp}	0	free	0	free	Cloud peak optical depth; amplitude in Fig. 1.
C _{press}	...	free	...	free	Pressure where the cloud layer is centered.
C _{vert}	...	free	...	free	Vertical extent of the clouds (bar).
<i>Physical properties</i>					
g _{surf} (cm s ⁻²)	free	free	free	free	Surface gravity, log(g _{surf}) ∈ (3.5, 5.2).
T ₁ – T ₉ (K)	free	free	free	free	Temperatures throughout the atmosphere.
<i>Calibration</i>					
A _{calib}	free	free	free	free	Multiplicative offset (poor absolute calibration).

^a Cloud-free, including only the four main molecules.

^b Cloudy, including only the four main molecules.

^c Cloud-free, including all seven molecules.

^d Cloudy, including all seven molecules.

companions for accurate atmospheric composition determination. These states are permitted in our simplified model fitting framework that does not impose any restrictions from atmospheric heat transport or chemical equilibrium. Were they the majority or a large fraction of all MCMC states, especially in case 1, we would conclude that the observed spectrum does not contain sufficient information to constrain the atmospheric properties using our approach. However, they constitute a minority of the MCMC states. Thus, we conclude that the inverted P-T profile states have little influence on our final results.

We estimate uncertainties and adopt best fit values based on the histograms of the MCMC parameter states. Even though we adopt the case 1 converged parameter values for our discussion based on the BIC values for the best fit models from the four cases, we present the results for both the cloudy and cloud-free models in the Appendix (Table 4 and Figures 8, 9 and 10).

We are able to estimate the volume mixing ratio of water molecules and we show the cloud-free water abundance histograms in Figure 4 for case 1, although the results are consistent between cases (Table 4). The case 1 histogram for CH₄ is flat, indicating poor convergence, but has a sharp peak and then cut-off towards higher number fractions. The cut-offs is well below the maximum value of 0.1 permitted in the MCMC. Thus, we place upper limits on the abundance of CH₄ by reporting the number density value below which 95% of MCMC iterations have occurred for that parameter. The abundances of CO and CO₂ remain unconstrained. The water volume mixing ratio and the upper limit for methane’s volume mixing ratio are consistent with predictions by Hubeny & Burrows (2007) for brown dwarfs, and with estimates by Heng & Lyons (2016) for C/O=0.5

at P = 1 bar, assuming solar metallicity.

Both CO and CO₂ have absorption bands in the 1 to 1.8 μm range, but these bands are weak, compared to water at these temperatures and pressures (HITEMP database Rothman et al. 2010), therefore, it is not surprising that these species, along with C₂H₂, HCN, NH₃ have little impact on our results, and especially the measured water volume mixing ratio. For all cloudy and cloud-free models, the water fractions are consistent with each other suggesting that clouds do not dominate the emission spectrum of the companion at this wavelength range, in the context of our simple cloud model.

The P-T profiles we present in Figure 3 do not encompass all of the nine levels in pressure where the temperature is a free parameter. The temperatures at altitudes above the ~ 0.1 bar level do not converge, since these layers are physically located well above the part of the atmosphere where the optical depth is close to 1, for all wavelengths between 1 and 1.8 μm.

6.2. Plausibility of Grey Clouds

Our main result, the volume mixing ratio of water is consistent between clear and grey cloud models, with and without the inclusion of additional molecules. Within our framework, grey clouds are not required to explain the observed spectrum, but cannot be excluded in principle. In order to check the physical plausibility of grey clouds consisting of large particles, we use typical values to estimate the thermal velocity of the gas in the atmosphere and the “eddy mixing strength” (or K_{zz}; e.g., Heng & Demory 2013) to be K_{zz} > 10⁹ – 10¹⁰. This value, compared to K_{zz} ~ 10⁴ that Marley et al. (2012) find for HR 8799b, is likely unphysical, suggesting that

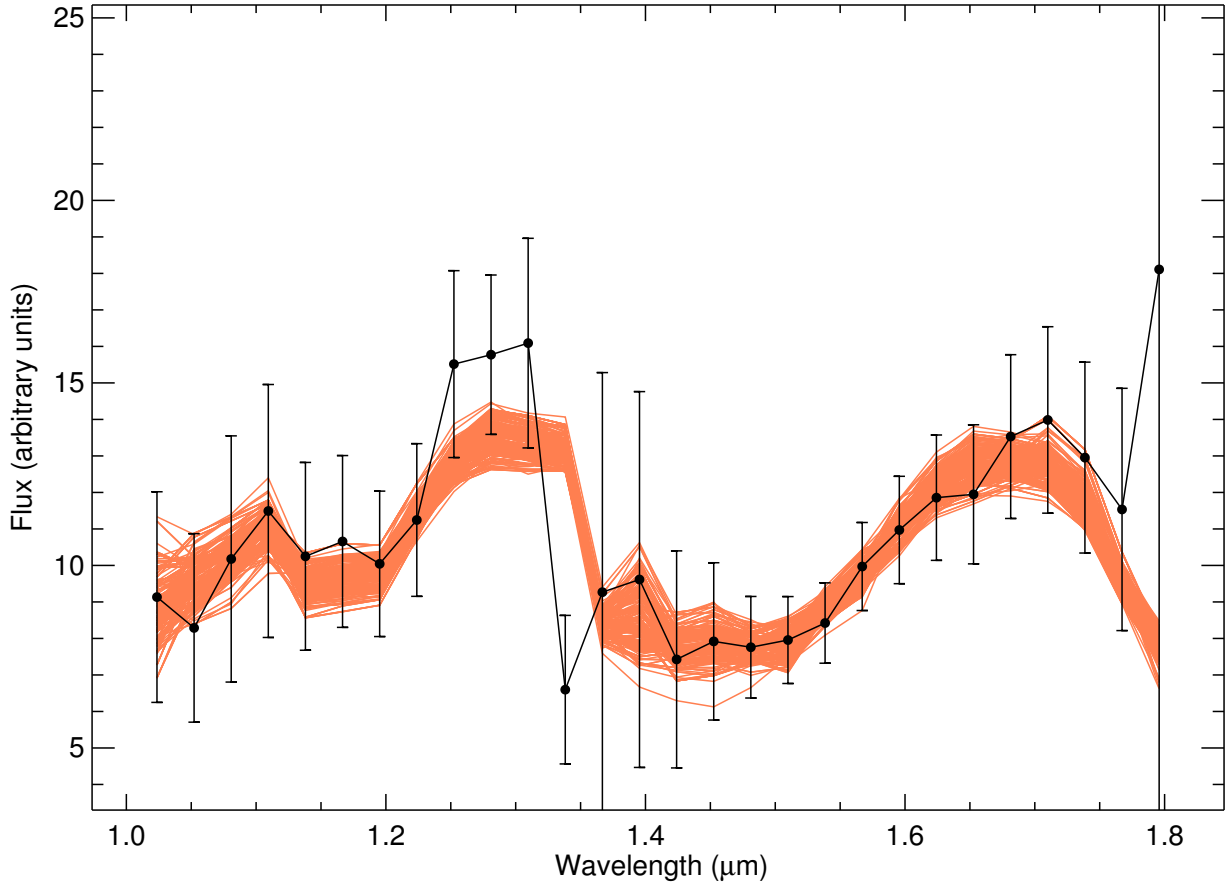


Figure 2. We compare about 300 instances of the model cloud-free four-core-molecule MCMC run (orange lines) to the observed spectrum of κ And b (connected black points; Hinkley et al. 2013). Each shown model is randomly chosen from a set with $\Delta\chi^2 < 1$ compared to the model with minimum $\chi^2 = 16.1$ ($\chi^2_{\text{reduced}} = 1.25$). The water absorption feature at $1.4 \mu\text{m}$ is clearly seen in the spectrum. While we plot absolute units on the vertical axis, the absolute calibration of the spectrum was poor in the original observations (unlike the relative calibration at different wavelengths). Thus, the ordinate axis here should be used to compare the difference of the fluxes at different bands and not the absolute flux of κ And b. The details of the observed spectrum and its uncertainties are discussed in Section 3.

the large-particle, grey-cloud assumption is too simplistic. However, there are proposed cloud compositions for which the grey assumption holds approximately over the relatively narrow wavelength range covered by our data, e.g., Na_2S (Morley et al. 2012) and MgSiO_3 , (Lee et al. 2013) even for smaller particle sizes, comparable to the radiation wavelength.

6.3. Comparison with Other Planets

We compare the water abundance we retrieve for κ And b based on case 1 with retrieved water abundances from other studies in Figures 6 and 7. Most of the points presented in these plots assume clear cloud-less models. Despite that, there are possible heterogeneities in the water volume mixing ratio determination due to different assumptions, as well as due to the different methods used to obtain spectral information. There are also possible heterogeneities related to the temperature determination. All hot Jupiters' temperatures given in Figure 6 are day side equilibrium temperatures based on distance to the star and stellar luminosity and assuming no redistribution to the night side of the planet. For the two directly imaged objects, HR 8799b and κ And b we adopt the effective temperatures found by Hinkley et al. (2013) and Lee et al. (2014b).

The water volume mixing ratio in the atmosphere of

κ And b is similar to the retrieved values from the day side emission of the transiting hot Jupiters TrES-2b ($1.3 M_J$), TrES-3b ($1.9 M_J$) and HD 149026b ($0.36 M_J$, Southworth 2010), as Figures 6 and 7 suggest (Line et al. 2014). These three hot Jupiters have day side equilibrium temperatures of $\sim 1930, 1920$ and 2110 K, respectively, which is similar to the effective temperature of 2040 ± 60 K for κ And b (Hinkley et al. 2013). This is despite the fact that κ And b is likely more massive than all three of these, and in fact than any of the other objects presented in Figures 6 and 7. The water volume mixing ratio of κ And b falls within the range of hot Jupiter abundances, although the uncertainties in the water abundances of the transiting planets are far larger than those for the directly imaged planets. We attribute this to the fact that in most cases the model retrieval on secondary eclipse data relied on multiband photometry of the planetary day side rather than spectroscopy. In addition, directly imaged spectra do not suffer from systematic effects resulting from eclipse and transit depth measurements. The wide range of water abundances covered by the companions in Figures 6 and 7 provides no proof that the amount of water in a companion's atmosphere is correlated with its temperature, irradiation level or mass. However, this may change as data with higher signal-to-noise ratio and with better spectral resolution

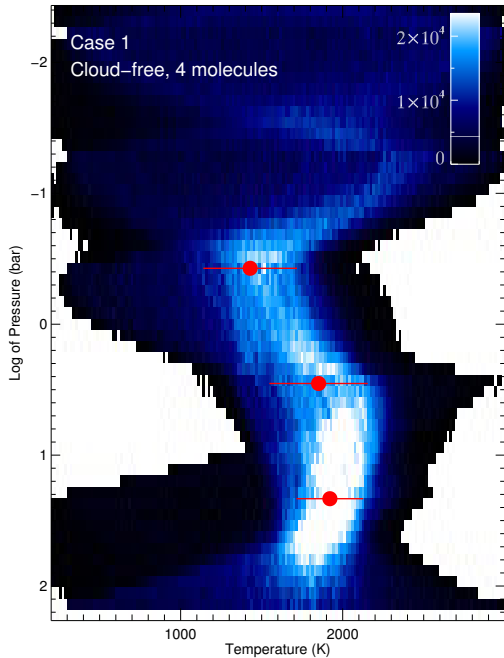


Figure 3. Histogram of the temperature values at each pressure level from the MCMC run for case 1: without clouds and only including CH_4 , CO , CO_2 and H_2O . The best-fit temperatures at pressures corresponding to the $T_1 - T_9$ free parameters are shown as red points with error bars. The uncertainties are based on the corresponding MCMC histograms. We define temperature parameters with uncertainties larger than 500 K as unconstrained (not shown).

Table 3
Results from the Case 1
MCMC Run

Parameter ^a	Best Value ^b
$\log(n_{\text{H}_2\text{O}})$	$-3.5^{+0.3}_{-0.6}$
$\log(n_{\text{CH}_4})^c$	< -2.6
$\log(n_{\text{CO}})$	no constraint
$\log(n_{\text{CO}_2})$	no constraint
T_6 (K) ^d	1430 ± 290
T_7 (K)	1850 ± 300
T_8 (K)	1920 ± 210
χ_{red}^2 ^e	1.25
BIC ^f	66.1

^a The parameter symbols are defined in Table 2.

^b Parameter values based on the MCMC run with no clouds and only the four main molecules: CH_4 , CO , CO_2 and H_2O .

^c 95% upper limits based on the MCMC histograms for these parameters.

^d Temperature parameters T_1 through T_5 and T_9 are unconstrained. We define the temperature parameter to be “constrained” if the 1σ uncertainties from the MCMC run are less than 500 K.

^e The reduced χ^2 value of the best fit model from the MCMC run.

^f The Bayesian Information Criterion value of the best fit model from this MCMC run.

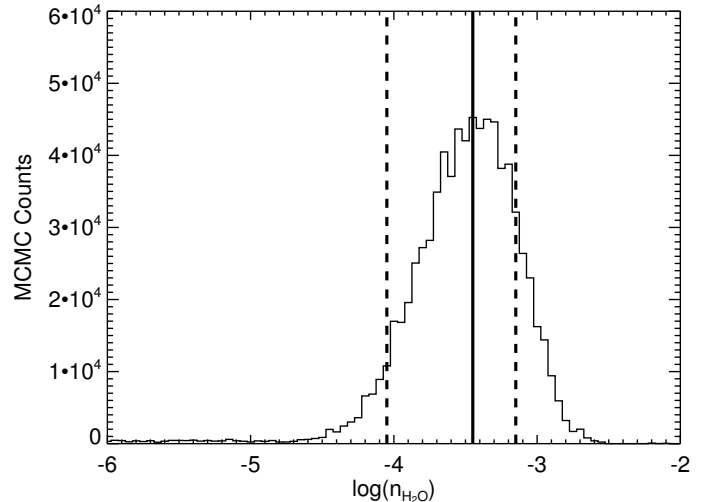


Figure 4. The histogram of cloud-free MCMC parameter states for the molecular number fraction of water in log space for the cloud-free case, including only the four main molecules (case 1). The MCMC histogram peaks strongly near $\log(n_{\text{H}_2\text{O}}) = -3.5$. We denote the peak of the distribution for case 1 (solid line) and the region that covers 34% (“ 1σ ”) of the values on either side (dashed lines).

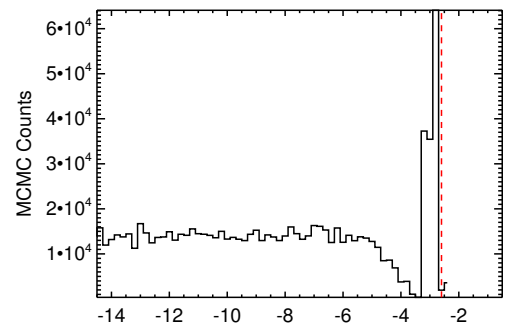


Figure 5. Similar to Figure 4 but for the CH_4 volume mixing ratio for the cloud-free, four molecules case (case 1). Despite the peak near $\log(n_{\text{CH}_4}) \approx -2.5$, the long tail towards very low abundances is pronounced, making it difficult to constrain the abundance of methane precisely. The red dashed line corresponds to the 95% upper limit on the number fraction.

and coverage become available for the objects, allowing for more precise abundance measurements.

7. SUMMARY AND FUTURE WORK

We find that the water abundance we derive for κ And b is not qualitatively different from these properties derived from the day side spectra and photometry of transiting hot Jupiters, although there is a wide range of water abundances that are currently consistent with the hot Jupiter measurements. Since H_2O is essential in the formation of the C/O ratio of an atmosphere, the similar water abundances may point to a common formation mechanism and location within the protoplanetary disk, followed by migration (e.g. Öberg et al. 2011; Madhusudhan et al. 2014a). This suggestion can be tested as the quality of secondary eclipse and direct imaging observations improves. Therefore, studying the molecular abundances of gas giant planets and companion brown dwarfs with very different effective temperatures, irradiation levels and masses that currently appear to inhabit a similar region of parameter space, is a logical next step.

Future development of our computational approach

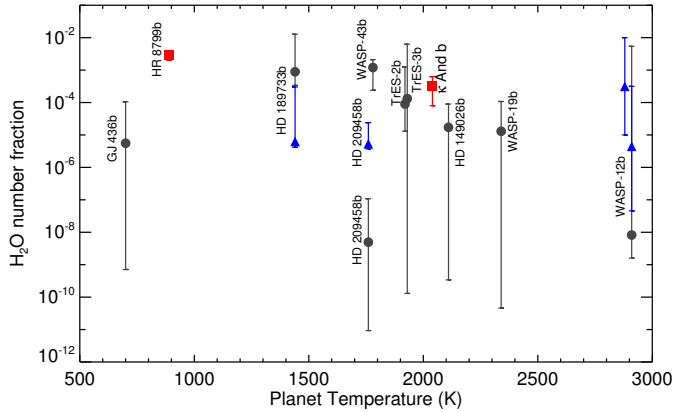


Figure 6. We compare the retrieved water abundances in the atmospheres of several hot giant planets with their temperatures. The retrieved water abundances of hot Jupiters based on secondary eclipse photometry and emission spectroscopy by [Line et al. \(2014\)](#) are shown as black circles (for WASP-43b we use the updated value from [Kreidberg et al. 2014](#)). The blue triangles without a label represent the water abundances of three planets from the [Line et al. \(2014\)](#) sample based on transit spectroscopy retrieval analysis by [Madhusudhan et al. \(2014b\)](#) and [Kreidberg et al. \(2015\)](#). The two points representing directly imaged companions (this work and [Lee et al. 2014b](#)) are shown as red squares. The value we show for κ And b is based on the cloud-free models that only include the abundances of CH_4 , CO , CO_2 and H_2O as free parameters, other than the P-T profile and the surface gravity (case 1). [Line et al. \(2014\)](#) and [Madhusudhan et al. \(2014b\)](#) also make the no-clouds assumption, unlike [Kreidberg et al. \(2014\)](#) and [Lee et al. \(2014b\)](#). For this plot, we use the equilibrium dayside temperatures for the hot Jupiters, assuming no redistribution to their night sides, and the effective temperatures for the directly imaged objects ([Hinkley et al. 2013](#); [Lee et al. 2014b](#)). The uncertainties of the abundance of water in the hot Jupiters based on secondary eclipse measurements are typically large since most of them have only dayside photometry in the mid-infrared and no spectroscopy, while the retrievals by [Madhusudhan et al. \(2014b\)](#) and those for HR 8799b and κ And b relied on near-infrared spectra. This suggests that the way to maximize precision in water abundance measurements is to rely on spectra of directly imaged companions. The coolest “hot Jupiter” on the plot, GJ 436b, is in fact a Neptune-sized planet orbiting a red dwarf on a 2.6 day orbit. The uncertainties on the water abundance of HR 8799b are too small to be clearly displayed in this logarithmic scale.

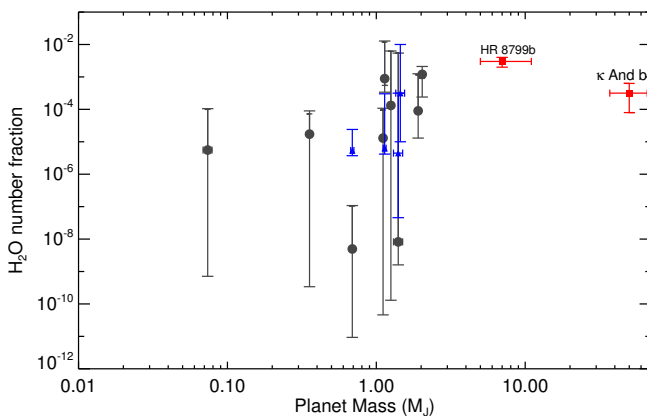


Figure 7. Similar to Figure 6, but here we compare the water volume mixing ratio to the mass of the planets and substellar companions. We adopt the masses listed in the The Extrasolar Planets Encyclopaedia^a, except for κ And b, for which we use the mass of $50^{+16}_{-13} M_J$ found by [Hinkley et al. \(2013\)](#). Again, we see no obvious dependence of water abundance on the mass of the planet.

^a<http://exoplanet.eu/>

will include proper treatment and weighting of photometric data points in addition to spectroscopy, which will allow full usage of all available data for a given substellar companion. While our spectrum contains 28 data points, which is a rich data set compared to many other exoplanet studies, it is still not a high-resolution, high-signal-to-noise spectrum. Obtaining higher quality spectra of directly imaged companions using the new generation of high-contrast instruments like GPI (Gemini South, [Macintosh et al. 2014](#)) and SPHERE (VLT, [Beuzit et al. 2008](#)) would allow for better constraints of their P-T profiles in a wider range of pressures and allow for better quantitative comparisons to the P-T profiles of hot Jupiters.

While the atmospheric emission model presented here is simplified and could yield unphysical results by not taking into account potentially important chemical species or physical processes, it is important to consider *along* with sophisticated, but computationally expensive, forward models. Our relatively fast code can account for and place uncertainties on the most important constituents of an atmosphere that shape the observed emission spectrum. The results from this and similar studies could be used as input for forward models that include additional physical and chemical considerations.

K.O.T., M.R.M. and S.P.Q. gratefully acknowledge the support of the Swiss National Centers of Competence in Research (NCCR) PlanetS initiative, funded by the Swiss National Science Foundation. This research has made use of NASA’s Astrophysics Data System. This research has made use of the Exoplanet Orbit Database and the Exoplanet Data Explorer at exoplanets.org. This research has benefitted from the SpeX Prism Spectral Libraries, maintained by Adam Burgasser at <http://pono.ucsd.edu/~adam/browndwarfs/spexprism>.

Table 4
Results from all MCMC Runs

Parameter ^a	Case 1 ^b	Case 2	Case 3	Case 4
$\log(n_{\text{H}_2\text{O}})$	$-3.5^{+0.3}_{-0.6}$	$-3.3^{+0.5}_{-6.8}$	$-3.5^{+0.4}_{-7.8}$	$-3.5^{+0.6}_{-7.9}$
$\log(n_{\text{CH}_4})^c$	< -2.6	no constraint	< -2.4	no constraint
$\log(n_{\text{CO}})$	no constraint	no constraint	no constraint	no constraint
$\log(n_{\text{CO}_2})^c$	no constraint	no constraint	< -2.2	no constraint
$\log(n_{\text{C}_2\text{H}_2})^c$	< -2.4	< -2.6
$\log(n_{\text{HCN}})^c$	< -3.0	< -2.2
$\log(n_{\text{NH}_3})^c$	< -3.0	< -2.6
T_6 (K) ^d	1430 ± 290	no constraint	no constraint	no constraint
T_7 (K)	1850 ± 300	no constraint	no constraint	no constraint
T_8 (K)	1920 ± 210	no constraint	2050 ± 230	no constraint
χ_{red}^2 ^e	1.25	2.21	1.13	2.06
BIC ^f	66.1	82.1	71.3	84.4

^a The parameter symbols are defined in Table 2.

^b Cases: 1) cloud-free and only the four main molecules; 2) cloudy and only with the four main molecules; 3) cloud-free, including the four main molecules plus the three additional ones; and 4) cloudy, with all seven considered molecules.

^c 95% upper limits based on the MCMC histograms for these parameters.

^d Temperature parameters $T_1 - T_5$ and T_9 are never constrained. We assume that a temperature parameter is “constrained” if the 1σ uncertainties from a given MCMC run are less than 500 K.

^e The reduced χ^2 value of the best fit model from this MCMC run.

^f The Bayesian Information Criterion value of the best fit model from this MCMC run.

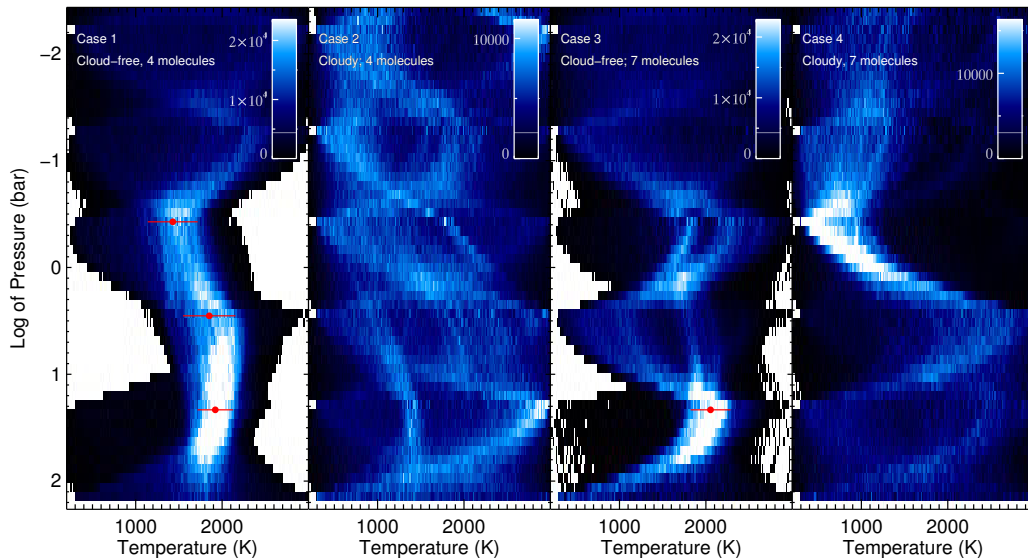


Figure 8. Histograms of the temperature values at each pressure level from the MCMCs for all four considered cases: 1) without clouds and only including the four main molecules: CH_4 , CO , CO_2 and H_2O ; 2) cloudy and only including the four main molecules; 3) cloud-free, including the four main molecules plus the three additional ones: C_2H_2 , HCN , NH_3 ; and 4) cloudy and all seven considered molecules. The red points with error bars represent the best-fit temperatures at pressures where corresponding to the $T_1 - T_9$ free parameters. The uncertainties are based on the corresponding MCMC histograms. We consider temperature parameters with uncertainties larger than 500 K be unconstrained and we do not plot these.

APPENDIX

MCMC RESULTS FOR ALL CASES

Here we present the results from the MCMC runs for all four cases that we explore. Table 4 lists the best fit values for all converged physical parameters. Figure 8 is similar to Figure 3 but shows the temperatures for all cases, not just for case 1. Figures 9 and 10 show the volume mixing ratio histograms for water and methane for each of the four cases. Even if we had adopted case 3 or case 4 that find upper limits on the number densities of C_2H_2 , HCN and NH_3 these would not have been meaningful, since these molecules are not expected to be present in such large quantities in the atmosphere of κ And b. The fact that the MCMC fits place an upper limit on these values simply confirms that these molecules play little role in the formation of the emission spectrum at this resolution.

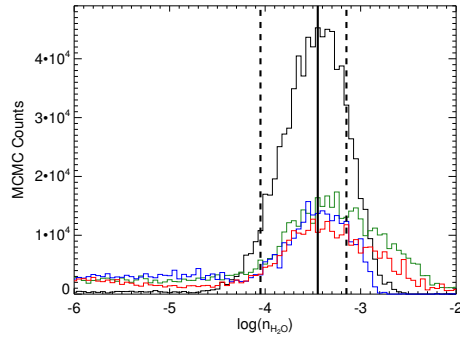


Figure 9. The histograms of cloud-free MCMC parameter states for the molecular number fraction of water in log space for each of the four cases we consider: cloud-free and only including the four main molecules (case 1; black); cloudy and only including the four main molecules (case 2, green); cloud-free, including all seven molecules (case 3, blue); and cloudy and including all seven molecules (case 4, red). All MCMC histograms peak near $\log(n_{\text{H}_2\text{O}}) \approx -3.5$, but the cloudy or seven-molecule models have long tails towards very low abundances. We denote the peak of the distribution for case 1 (solid black line) and the region that covers 34% (“1 σ ”) of the values on either side (dashed black lines).

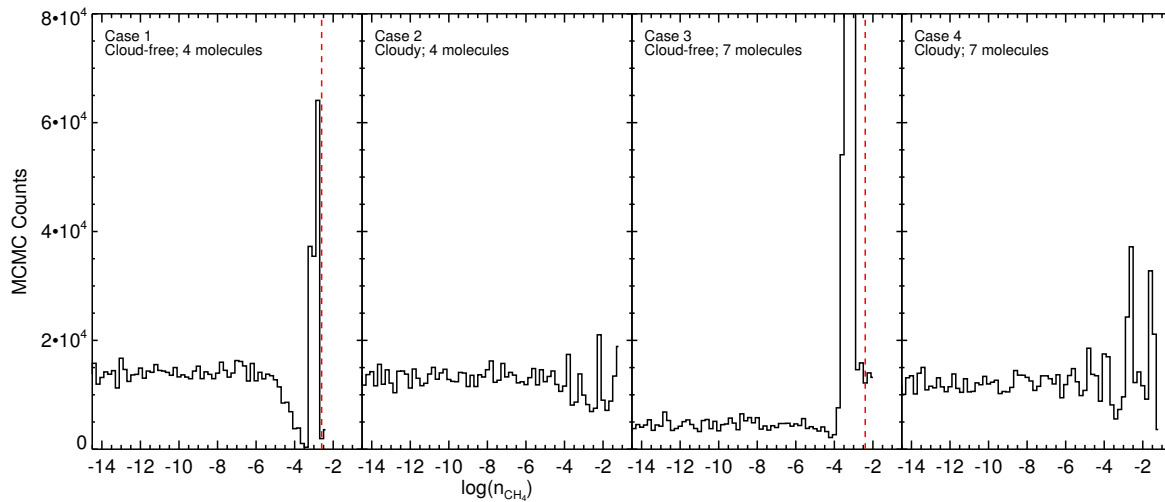


Figure 10. Similar to Figure 9 but for the CH_4 volume mixing ratios. The four panels show the MCMC histograms for the four model cases labeled. In the cloudy cases the methane abundance is unconstrained. In the cloud-free cases, have peaks near $\log(n_{\text{CH}_4}) \approx -2.5$, but their long tails towards very low abundances are pronounced. The red dashed lines correspond to the 95% upper limits on the number fraction of CH_4 in the cloud-free models.

REFERENCES

- Allard, F., Homeier, D., & Freytag, B. 2011, 16th Cambridge Workshop on Cool Stars, Stellar Systems, and the Sun, 448, 91 [2](#)
- Benneke, B., & Seager, S. 2012, *ApJ*, 753, 100 [1](#)
- Benneke, B., & Seager, S. 2013, *ApJ*, 778, 153 [1](#)
- Bertelli, G., Nasi, E., Girardi, L., & Marigo, P. 2009, *A&A*, 508, 355 [2](#)
- Beuzit, J.-L., Feldt, M., Dohlen, K., et al. 2008, *Proc. SPIE*, 7014, 701418 [7](#)
- Bonnefoy, M., Currie, T., Marleau, G.-D., et al. 2014, *A&A*, 562, AA111 [2](#)
- Borysow, A., Jorgensen, U. G., & Fu, Y. 2001, *J. Quant. Spec. Radiat. Transf.*, 68, 235 [4.1](#)
- Borysow, A. 2002, *A&A*, 390, 779 [4.1](#)
- Burrows, A., Hubeny, I., Budaj, J., Knutson, H. A., & Charbonneau, D. 2007, *ApJ*, 668, L171 [1](#)
- Burrows, A., Budaj, J., & Hubeny, I. 2008, *ApJ*, 678, 1436 [1](#)
- Burrows, A., Heng, K., & Nampaisarn, T. 2011, *ApJ*, 736, 47 [4.2](#)
- Carson, J., Thalmann, C., Janson, M., et al. 2013, *ApJ*, 763, LL32 [1](#), [2](#), [3](#), [1](#)
- Sheppard, S. S., & Cushing, M. C. 2009, *AJ*, 137, 304 [4.1](#)
- Freedman, R. S., Lustig-Yaeger, J., Fortney, J. J., et al. 2014, *ApJS*, 214, 25 [4.1](#)
- Ford, E. B. 2005, *AJ*, 129, 1706 [5.2](#)
- Ford, E. B. 2006, *ApJ*, 642, 505 [5.2](#)
- Fortney, J. J., Cooper, C. S., Showman, A. P., Marley, M. S., & Freedman, R. S. 2006, *ApJ*, 652, 746 [1](#)
- Fortney, J. J., Marley, M. S., Saumon, D., & Lodders, K. 2008, *ApJ*, 683, 1104 [1](#)
- Gray, D. F. 2005, *The Observation and Analysis of Stellar Photospheres* (3rd ed.; Cambridge, UK: Cambridge University Press) [4.1](#)
- Heng, K., Hayek, W., Pont, F., & Sing, D. K. 2012, *MNRAS*, 420, 20 [4.2](#)
- Heng, K., & Demory, B.-O. 2013, *ApJ*, 777, 100 [6.2](#)
- Heng, K., & Lyons, J. R. 2016, *ApJ*, 817, 2 [1](#), [6.1](#)
- Hinkley, S., Oppenheimer, B. R., Zimmerman, N., et al. 2011, *PASP*, 123, 74 [3](#)
- Hinkley, S., Pueyo, L., Faherty, J. K., et al. 2013, *ApJ*, 779, 153 [1](#), [2](#), [3](#), [1](#), [5.1](#), [2](#), [6.3](#), [6](#), [7](#)
- Hubeny, I., & Burrows, A. 2007, *ApJ*, 669, 1248 [6.1](#)
- Irwin, P. G. J., Teanby, N. A., de Kok, R., et al. 2008, *J. Quant. Spec. Radiat. Transf.*, 109, 1136 [4.1](#)

- Kreidberg, L., Bean, J. L., Désert, J.-M., et al. 2014, *ApJ*, 793, LL27 6
- Kreidberg, L., Line, M. R., Bean, J. L., et al. 2015, *ApJ*, 814, 66 6
- Lee, J.-M., Fletcher, L. N., & Irwin, P. G. J. 2012, *MNRAS*, 420, 170 1
- Lee, J.-M., Heng, K., & Irwin, P. G. J. 2013, *ApJ*, 778, 97 1, 4.2, 6.2
- Lee, J.-M., Irwin, P. G. J., Fletcher, L. N., Heng, K., & Barstow, J. K. 2014a, *ApJ*, 789, 14 1, 3, 4.2
- Lee, J.-M., Heng, K., & Irwin, P. G. J. 2014b, *ApJ*, 780, 190 1, 4.2, 6.3, 6
- Line, M. R., Zhang, X., Vasisht, G., et al. 2012, *ApJ*, 749, 93 1, 4.1, 4.1
- Line, M. R., Wolf, A. S., Zhang, X., et al. 2013, *ApJ*, 775, 137 1, 4.1, 4.1
- Line, M. R., Knutson, H., Wolf, A. S., & Yung, Y. L. 2014, *ApJ*, 783, 70 6.3, 6
- Lodders, K., & Fegley, B. 2002, *Icarus*, 155, 393 4.1
- Macintosh, B., Graham, J. R., Ingraham, P., et al. 2014, *Proceedings of the National Academy of Science*, 111, 12661 7
- Madhusudhan, N., Burrows, A., & Currie, T. 2011, *ApJ*, 737, 34 1
- Madhusudhan, N., Amin, M. A., & Kennedy, G. M. 2014a, *ApJ*, 794, LL12 1, 7
- Madhusudhan, N., Crouzet, N., McCullough, P. R., Deming, D., & Hedges, C. 2014b, *ApJ*, 791, LL9 6
- Markwardt, C. B. 2009, in *ASP Conf. Ser. 411, Astronomical Data Analysis Software and Systems XVIII*, ed. D. A. Bohlender, D. Durand, & P. Dowler (San Francisco, CA: ASP), 251 5.2
- Marley, M. S., Saumon, D., Cushing, M., et al. 2012, *ApJ*, 754, 135 6.2
- Marois, C., Zuckerman, B., Konopacky, Q. M., Macintosh, B., & Barman, T. 2010, *Nature*, 468, 1080 2
- Morley, C. V., Fortney, J. J., Marley, M. S., et al. 2012, *ApJ*, 756, 172 4.2, 6.2
- Öberg, K. I., Murray-Clay, R., & Bergin, E. A. 2011, *ApJ*, 743, LL16 1, 7
- Oppenheimer, B. R., Beichman, C., Brenner, D., et al. 2012, *Proc. SPIE*, 8447, 844720 3
- Pepe, F., Ehrenreich, D., & Meyer, M. R. 2014, *Nature*, 513, 358 1
- Perryman, M. A. C., Lindgren, L., Kovalevsky, J., et al. 1997, *A&A*, 323, L49 3, 1
- Rothman, L. S., Gordon, I. E., Barber, R. J., et al. 2010, *JQSRT*, 111, 2139 4.1, 6.1
- Rothman, L. S., Gordon, I. E., Barbe, A., et al. 2009, *JQSRT*, 110, 533 4.1
- Skrutskie, M. F., Cutri, R. M., Stiening, R., et al. 2006, *AJ*, 131, 1163 1
- Southworth, J. 2010, *MNRAS*, 408, 1689 6.3
- Swain, M. R., Vasisht, G., Tinetti, G., et al. 2009, *ApJ*, 690, L114 4.1
- Tinetti, G., Liang, M.-C., Vidal-Madjar, A., et al. 2007, *ApJ*, 654, L99 4.1
- Todorov, K. O., Deming, D., Knutson, H. A., et al. 2012, *ApJ*, 746, 111 5.2
- Todorov, K. O., Deming, D., Burrows, A., & Grillmair, C. J. 2014, *ApJ*, 796, 100 5.2
- Wu, Y., Singh, H. P., Prugniel, P., Gupta, R., & Koleva, M. 2011, *A&A*, 525, AA71 2, 1
- Zahnle, K. J., & Marley, M. S. 2014, *ApJ*, 797, 41 4.1
- Zuckerman, B., Rhee, J. H., Song, I., & Bessell, M. S. 2011, *ApJ*, 732, 61 2